ACS Catalysis

Research Article

pubs.acs.org/acscatalysis

In Situ Surface Chemistries and Catalytic Performances of Ceria Doped with Palladium, Platinum, and Rhodium in Methane Partial Oxidation for the Production of Syngas

Yuan Zhu,† Shiran Zhang,† Jun-jun Shan,† Luan Nguyen, Sihui Zhan, Xiaoli Gu, and Franklin (Feng) Tao*

Department of Chemistry and Biochemistry, University of Notre Dame, Notre Dame, Indiana 46556, United States

Supporting Information

ABSTRACT: Methane partial oxidation (MPO) chemically transforms natural gas into syngas for the production of gasoline. CeO_2 doped with transition-metal ions is one type of catalyst active for MPO. A fundamental understanding of MPO on this type of catalyst is important for the development of catalysts with high activity and selectivity for this process. CeO_2-based catalysts, including Pd-CeO_2-air, Pd-CeO_2-H_2, Pt-CeO_2-air, Pt-CeO_2-H_2, Rh-CeO_2-air, and Rh-CeO_2-H_2, were synthesized through doping noble-metal ions in the synthesis of CeO_2 nanoparticles. The catalytic activity and selectivity in the production of H_2 and CO through MPO on these ceria-based catalysts as well as their surface chemistries during catalysis were investigated. They exhibit quite different catalytic performances in MPO under identical catalytic conditions. In situ studies of their surface chemistries during catalysis, using ambient-pressure X-ray photoelectron spectroscopy (AP−XPS), revealed quite different surface chemistries during catalysis. Correlations between the catalytic performances of these catalysts and their corresponding surface chemistries during catalysis were developed. Differing from the other four catalysts, Rh doped in the surface lattice of a CeO_2 catalyst, including Rh-CeO_2-air and Rh-CeO_2-H_2, is in a complete ionic state during catalysis. Correlations between the in situ surface chemistry and the corresponding catalytic performance show that Rh ions and Pt ions doped in the lattice of CeO_2 as well as metallic Pd nanoparticles supported on CeO_2 are active components for MPO. Among these catalysts, Rh-doped CeO_2 exhibited the highest catalytic activity and selectivity in MPO.

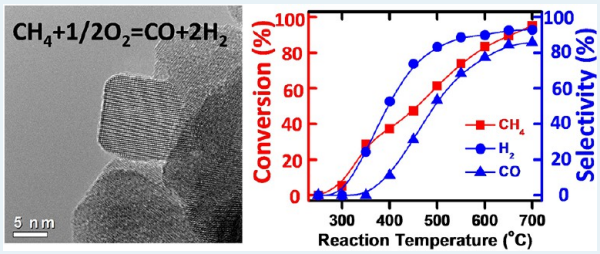

KEYWORDS: *in situ, methane partial oxidation, ceria, ambient-pressure XPS, synthesis*

1. INTRODUCTION

In contrast to crude oil, natural gas is relatively abundant even if the methane generated from biomass and the methane hydrate from seashells are not taken into account. One utilization of natural gas is the production of gasoline from synthesis gas (syngas) through methane partial oxidation (MPO).[1−4] MPO is an economical strategy to generate syngas from natural gas.[4−33] The production of syngas through MPO using different catalysts has been studied in the past decades.[34] Several groups[35−39,42,47] have studied methane activation over CeO_2 either doped or impregnated with precious metals. For example, Pt-doped CeO_2 catalysts were prepared with several methods including coprecipitation,[40] impregnation,[41−46] deposition−precipitation,[47] sol−gel,[47] and flame combustion.[40,42,47] It was proposed that doping a reducible oxide with noble-metal atoms could tune the catalytic activity of the oxide by shifting the Fermi level through integrating doped ions into the lattice of the oxide surface.[48] In addition, this doping could change the formation energy of oxygen vacancies and thus influence the reactivity of the oxygen atoms of the surface lattice of a reducible oxide toward the activation of C−H bonds.[47] The doping of Pt ions likely activates neighboring oxygen atoms and decreases the activation energy of C−H dissociation on oxygen atoms of the surface lattice.

Compared to Pt or Pd, Rh exhibits different binding energies to oxygen atoms.[49,50] A stronger binding of Rh ions to surface-lattice oxygen atoms upon the doping of Rh ions could make Rh-doped CeO_2 exhibit a catalytic performance different from that of CeO_2 doped with Pd or Pt ions. Rh ions could activate oxygen atoms of the surface lattice and thus promote C−H dissociation significantly. Compared to Rh ions, Pd ions could be reduced to metallic Pd readily. Thus, it is expected that Pd-CeO_2 exhibits a different surface chemistry and catalytic performance for MPO. To understand how the different noble-metal ions/atoms influence the catalytic performance of MPO, it is necessary to perform parallel studies of CeO_2 catalysts doped with different cations, including Pd, Pt, and Rh. Although the catalytic performances of MPO on Pt-doped CeO_2 have been studied[47] and the surface chemistries of these catalysts have been characterized through ex situ approaches,

Received: January 28, 2013
Revised: September 11, 2013
Published: September 18, 2013

   dx.doi.org/10.1021/cs400070y | ACS Catal. 2013, 3, 2627−2639

there is a lack of a direct correlation between the in situ surface chemistry of catalysts during catalysis and their corresponding catalytic performance. Here, we used an ambient-pressure X-ray photoelectron spectrometer (AP−XPS) available in our group to track the surface chemistries of CeO_2 doped with Pd, Pt, and Rh ions during MPO at different temperatures because AP−XPS is an in situ technique with a high surface sensitivity.[51−54] Pd-CeO_2, Pt-CeO_2, and Rh-CeO_2 were synthesized with the same method. A pretreatment in air or H_2 resulted in six catalysts (Pd-CeO_2-air, Pd-CeO_2-H_2, Pt-CeO_2-air, Pt-CeO_2-H_2, Rh-CeO_2-air, and Rh-CeO_2-H_2) that were evaluated for their catalytic performance and their in situ surface chemistry during catalysis (using AP−XPS).

Here, the catalytic performances of the six catalysts were examined under the same catalytic conditions. Surface chemistries of these catalysts during catalysis were tracked with AP−XPS. Correlations between surface chemistry and the corresponding catalytic performance were developed. These correlations provide insight into the differences in catalytic performance. Insights achieved from these correlations are important for developing catalysts for MPO that have high activity and selectivity.

2. EXPERIMENTAL SECTION

2.1. Preparation of CeO_2-Based Catalysts Doped with 5% Pd, Pt, or Rh. A solution-based hydrothermal procedure[55] was used to prepare the Pd-, Pt-, and Rh-doped CeO_2 catalysts. $Ce(NO_3)_3{\cdot}6H_2O$ (1.7369 g, Sigma-Aldrich, 99% trace metals basis) and a metal precursor, 0.0561 g of $Pd(NO_3)_2{\cdot}2H_2O$, 0.1090 g of $H_2PtCl_6{\cdot}6H_2O$, or 0.0541 g of $RhCl_3$ (Sigma-Aldrich), were dissolved in 5 mL of deionized water simultaneously and added to 60 mL of a sodium hydroxide solution in a Teflon bottle. The mixture was filled to 80 mL, giving a final NaOH concentration of 6.0 M. This solution was stirred for 15 min to form a milky slurry. The slurry was subsequently transferred to a 100 mL Teflon-lined stainless steel autoclave and heated in an oven at 100 °C for 24 h. The autoclave was then cooled to room temperature. The product was collected in a beaker by self-sedimentation and was washed with deionized water. After decanting the supernatant until the pH value reached ∼7, the sample was dried at 100 °C. Calcination in air or H_2 resulted in the six different catalysts. Calcination at 500 °C in air offered catalysts Pd-CeO_2-air, Pt-CeO_2-air, and Rh-CeO_2-air. Calcination at 500 °C in 5% H_2/Ar provided catalysts Pd-CeO_2-H_2, Pt-CeO_2-H_2, and Rh-CeO_2-H_2. The concentration of Pd in Pd-CeO_2-air and Pd-CeO_2-H_2, of Pt in Pt-CeO_2-air and Pd-CeO_2-H_2, and of Rh in Rh-CeO_2-air and Pd-CeO_2-H_2 was measured with inductively coupled plasma atomic emission spectroscopy (ICP-AES, PerkinElmer Optima 3000XL) after the catalysis measurements. On the basis of the ICP-AES measurements, the doping levels of these reacted catalysts were 5.0 ± 0.3%, very close to the atomic ratio of Pd, Pt, or Rh to CeO_2 of 5.0% used in syntheses.

2.2. Powder X-ray Diffraction and Transmission Electron Microscopy. Powder X-ray diffraction (XRD) patterns of the six catalysts were acquired on a Bruker D8 Advance XRD using nickel-filtered Cu Kα radiation (λ = 1.5418 Å) operating at 40 kV and 40 mA in a continuous mode with a scanning rate of 4.2° min^{-1} in the 2θ range from 20° to 90°. The size, shape, and lattice fringe of the CeO_2-doped catalysts were identified using high-resolution transmission electron microscope (FEI, Titan 80-300) operated at an accelerating voltage of 300 kV. Image analyses were performed with Digital Micrograph (Gatan) software. TEM samples were prepared by grinding the catalyst with an agate mortar, dispersing 10 mg of the sample in 1 mL of anhydrous ethanol, sonicating it for 10 min, and finally dropping the solution to a lacey-carbon-film-coated 200 mesh copper grid (Electron Microscopy Sciences).

2.3. Measurements of Catalytic Performance. Measurements of the catalytic activity and selectivity of these catalysts for MPO were carried out at atmospheric pressure in a fixed-bed tubular quartz microreactor (i.d. = 6 mm, length = 300 mm). One hundred milligrams of a sieved catalyst sample (40−60 mesh) diluted with quartz sand (the bed height was ca. 5 mm) was packed in between two quartz wool plugs. The catalyst was heated in a furnace equipped with a proportional-integral-derivative (PID) temperature controller (Across International). Pretreatment of the as-synthesized catalyst M-CeO_2 in air was performed at 500 °C for 3 h in a muffle furnace (Across International). Before catalytic experiments using the M-CeO_2-air catalyst, it was flushed with pure Ar (99.99%, Praxair, Inc.) for 30 min and then exposed to the reactant gases flowing at a rate of 100 mL min^{-1} (controlled by a Dakota Instruments, Inc. mass flow meter/controller). The gas composition of the mixture of reactant gases was 5% CH_4, 2.5% O_2, and 92.5% Ar (Praxair, Inc.). For M-CeO_2-H_2, the catalyst precursor was pretreated in 5% H_2 at 500 °C (50 mL/min) for 3 h and then cooled to near room temperature naturally in 5% H_2. Upon switching to the mixture of reactant gases, the catalytic performance of M-CeO_2-H_2 for MPO was measured. For comparison, the catalytic performance of MPO on M-CeO_2-H_2 was measured under the same conditions as those used for M-CeO_2-air.

A cold trap downstream of the reactor outlet was used to condense the water formed during the reaction. The effluent gas was connected to a gas chromatograph (8610C, SRI Instruments) equipped with a HayeSep D (6′ × $^1/_8$″) packed column, a molecular sieve 13× (6′ × $^1/_8$″) packed column, and a thermal conductivity detector (TCD) for the analysis of both the reactants and products. In this work, the calculations for the conversion of methane (X_{CH_4}) and the selectivity of hydrogen (S_{H_2}) and carbon monoxide (S_{CO}) were calculated using the following equations

$$X_{CH_4}\ (\%) = [(C_{CH_4,\mathrm{inlet}} - C_{CH_4,\mathrm{outlet}})/C_{CH_4,\mathrm{inlet}}] \times 100$$

$$S_{H_2}\ (\%) = [\text{moles of } H_2 \text{ produced} / (2 \times \text{moles of } CH_4 \text{ consumed})] \times 100$$

$$S_{CO}\ (\%) = [\text{moles of CO produced} / \text{moles of } CH_4 \text{ consumed}] \times 100$$

where $C_{CH_4,\mathrm{inlet}}$ and $C_{CH_4,\mathrm{outlet}}$ are defined as the molar fractions of CH_4 at the reactor inlet and outlet, respectively.

2.4. In Situ Studies using Ambient-Pressure X-ray Photoelectron Spectroscopy. The surface chemistry of the six catalysts was studied using an in-house ambient-pressure X-ray photoelectron spectrometer (AP−XPS) with an Al Kα monochromator (Microfocus 600, Specs) and energy analyzer (Phoibos 150, Specs) in the Tao group.[56] In terms of the resolution of this spectrometer, the measured full-width at half-maximum (fwhm) of the Ag 3d 5/2 spectrum in UHV is 0.3 eV. XPS peaks were calibrated to Au 4f 7/2 at 84.0 eV and Ag 3d 5/2 at 368.3 eV.[57] Photoemission features of Ce 3d, Pt 4f,

dx.doi.org/10.1021/cs400070y | ACS Catal. 2013, 3, 2627−2639

Pd 3d, Rh 3d, and O 1s were tracked during catalysis at different temperatures. The interpretation of the photoemission features and the assignment of the binding energies of the photoelectrons excited from these subshells are based on references of Ce 3d,[57−59] Pt 4f,[57,60] Pd 3d,[57,61] Rh 3d,[57,62] and O 1s.[57] All Ce 3d spectra were deconvoluted by building four peaks of Ce^{3+} (u′, u_o, v′, and v_o) and six peaks of Ce^{4+} (u‴, u″, u, v‴, v″, and v) based on the peak positions of pure Ce_2O_3[59] and pure CeO_2 reported by Mullins et al.[59] and ref 63. Here, each Ce 3d spectrum was deconvoluted into 10 peaks, including 880.5 with a fwhm of 2.5 eV, 882.7 with a fwhm of 2.0 eV, 885.1 with a fwhm of 2.4 eV, 888.9 with a fwhm of 4.6 eV, 898.5 with a fwhm of 1.9 eV, 899.2 with a fwhm of 2.5 eV, 901.2 with a fwhm of 2.0 eV, 903.5 with a fwhm of 2.4 eV, 907.5 with a fwhm of 4.6 eV, and 916.3 with a fwhm of 1.9 eV. The details of the deconvolution of Ce 3d of the CeO_2 particles can be found in the Experimental Section and in the Supporting Information of a recent publication.[63] In the deconvolution of Pt 4f, the peak positions of Pt^0, Pt^{2+}, and Pt^{4+} were assigned with the peak positions reported in literature.[60] In addition, the fwhm of all components of the Pt 4f spectrum were constrained to be the same. In the fitting of Pd 3d, peak positions of Pd^0, Pd^{2+}, and Pd^{4+} were referred to the literature,[61] and all components maintained the same fwhm. Rh 3d spectra were deconvoluted by building components of Rh^{3+} and Rh^0 at the corresponding peak positions reported in the literature[62] and maintaining the same fwhm of each component.

All XPS data presented in this article were collected from catalysts at the listed temperature (25−600 °C) in a gas environment of reactants with a listed pressure (2 Torr CH_4 and 1 Torr O_2). A catalyst sample was installed into a sample stage located in the reaction cell for tracking the surface chemistry during catalysis. The sample was heated via conduction from an external wall of the reaction cell. The external wall of the sample stage was heated via the bombardment of electrons from an e-beam heater installed on the vacuum side of the reaction cell. The heating of the sample in the reaction cell is presented schematically in Figure S1.

To exclude any potential side reactions of the nickel in the stainless steel of the sample stage, we deliberately oxidized the sample stage. The oxidation was confirmed with XPS. The oxidation of the wall of the reaction cell excluded the participation of the nickel in the stainless steel in catalysis. In addition, the aperture was coated with a thick layer of graphite (about 0.1 mm or thicker) when we received it. Because of a thermal decomposition of the reactant CH_4 or the byproducts of the MPO at high temperature, the carbon dissociated from CH_4 or the byproducts of the MPO at high temperature could have accumulated on the aperture. Because Au and graphite were subsequently deposited on the aperture by the manufacturer, the buried nickel of the stainless steel of the aperture located below the graphite and Au thin films was not exposed to any gases.

The sample temperature was controlled through tuning the emission current of the filament of the e-beam heater. Reactant gases were introduced to the reaction cell through the entrance pore (Figure S1), flowed through the sample, and exited through both the exit pore (Figure S1) and the aperture adapted to a prelens. Gas pressure in the reaction cell was measured through averaging the readings of two gauges installed at the entrance and exit tubes of the reaction cell. The difference between the pressures at the entrance and exit of the reaction cell is less than 10−15%. The existence of the gas phase above the sample surface was confirmed by the observation of the N 1s photoemission peak from nitrogen atoms of N_2 at 405 eV duing a test of an Ag thin film in the nitrogen gas phase.[56] The pressure in the reaction cell was tuned through the mass flow meters installed on the tube for gas introduction and/or through the pumping rate at the exit of the reaction cell. Ce 3d, Pt 4f, Pd 3d, Rh 3d, and O 1s were tracked when the catalyst was in the gas mixture of pure CH_4 (2 Torr) and pure O_2 (1 Torr) at different temperatures.

The pressure of the reactant gas, a mixture of pure CH_4 and O_2 in a molar ratio of 2:1 around the catalyst in the reaction cell of our AP−XPS system, was 3 Torr during the in situ studies of the surface chemistry of these catalysts. In the experimental evaluation of the catalytic performance, 5% CH_4 was used. The partial pressure was about 38 Torr. Because we assume that the difference in the pressure of CH_4 in the reaction cell of the AP−XPS (3 Torr) and that in the reactor of catalysis test (38 Torr) does not result in a significant difference in the surface chemistry of a catalyst, the surface chemistry revealed with AP−XPS can represent that of the catalysts during catalysis in a flow reactor.

3. RESULTS AND DISCUSSION

3.1. Pd-Doped CeO_2. *3.1.1. Pd-CeO_2 at Room Temperature.* The as-synthesized catalyst (Pd-CeO_2) was pretreated in air or 5% H_2/Ar. Figure 1a presents TEM images of Pd-CeO_2 pretreated in air (termed Pd-CeO_2-air). There are not any identifiable nanoclusters on the surface of the Pd-CeO_2-air, showing that Pd ions were doped in the lattice of CeO_2 instead of the formation of PdO_x or Pd nanoparticles on CeO_2. The interplanar distances of CeO_2 doped with Pd ions (Pd-CeO_2-air) were measured in TEM studies. They are very close to pure CeO_2. The almost identical interplanar distance could partially result from the small difference between the ionic radius of Ce^{4+} (101 pm) and the doped ions (e.g., Pt^{2+} (94 pm), Pd^{2+} (100 pm), Pd^{4+} (75.5 pm), and Rh^{3+} (80.5 pm)).[64]

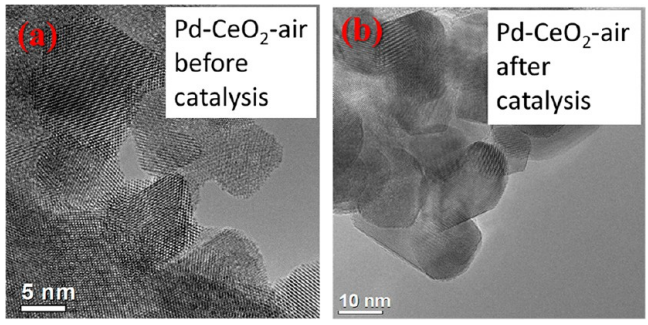

Figure 1. High-resolution TEM images of Pd-CeO_2-air before (a) and after (b) catalysis. The average size of CeO_2 doped with Pd is 13.0 nm based on a statistical accounting of the nanoparticles in the TEM images from different parts of the catalyst sample.

Figures 2a1 and 2b1 are the photoemission features of Pd 3d of Pd-CeO_2-air and Pd-CeO_2-H_2 in the mixture of reactants at room temperature. They represent the surface chemistry of Pd-CeO_2-air and Pd-CeO_2-H_2 before catalysis because Pd-CeO_2-air and Pd-CeO_2-H_2 are not active for MPO at room temperature. In the following section, we will use the surface chemistry of Pt-CeO_2-air, Pt-CeO_2-H_2, Rh-CeO_2-air, and Rh-CeO_2-H_2 at room temperature in the mixture of CH_4 and O_2 to represent their

dx.doi.org/10.1021/cs400070y | ACS Catal. 2013, 3, 2627−2639

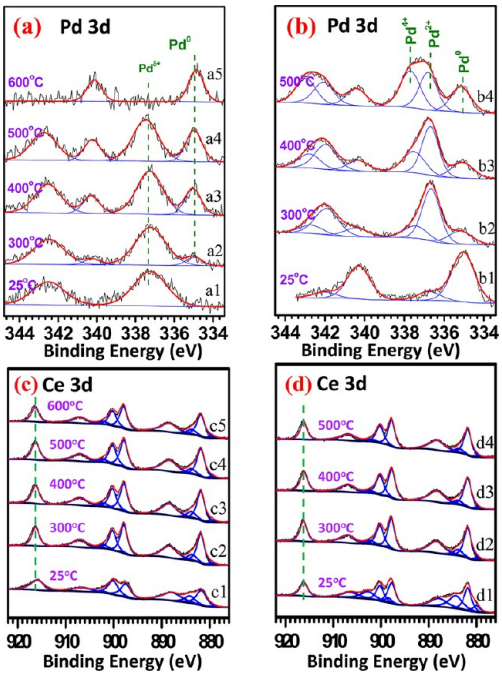

Figure 2. XPS spectra of the in situ studies of Pd 3d of Pd-CeO_2-air (a), Pd 3d of Pd-CeO_2-H_2 (b), Ce 3d of Pd-CeO_2-air (c), and Ce 3d of Pd-CeO_2-H_2 (d) during catalysis. The fwhm of the fitted peaks of Pd 3d in panels a and b were fixed at 1.4 and 1.2 eV, respectively. The ratio of the partial pressures of CH_4 to O_2 in the mixture reactant is 2:1, with a total pressure of 3 Torr. The flow rate is 6 mL min^{-1}. All AP–XPS data were collected at the same pressure and flow rate of CH_4 and O_2. The only variable is the reaction temperature. The spectra collected at 25 °C is used to represent the surface chemistry of the catalysts before catalysis because none of these catalysts is active for MPO at 25 °C.

surface chemistries before catalysis because none of them are active for MPO at room temperature.

It is noted that there is no charging for Pd 3d and Ce 3d of the sample at room temperature. The lack of charging is evidenced by the fact that the peak position u‴ of Ce 3d from Ce^{4+} at ~916.3 eV observed in Figure 2c1,d1 is identical to those reported in refs 59 and 63. Because a Ce 3d spectrum of CeO_2 is typically deconvoluted into six peaks of Ce^{4+} and four peaks of Ce^{3+},[59,63] the fraction of Ce^{3+} could largely influence the shape of the Ce 3d spectrum. For a Ce 3d spectrum of CeO_2 with a very low fraction of Ce^{3+}, there is one obvious valley at ~883 eV (Figure 2c2,d2). If the fraction of Ce^{3+}, ~30%, is relatively high, then the valley is filled by one peak of Ce^{3+} at 883 eV (Figure 2d1). Thus, the shape of Ce 3d spectrum cannot be used to judge whether there is charging or not.

Before the catalysis of MPO, Pd of Pd-CeO_2-air exists in an oxidized state (Figure 2a1) and exists mainly in a metallic state for Pd-CeO_2-H_2 at room temperature (Figure 2b1). The photoemission features of Pd 3d and Ce 3d at a temperature higher than 25 °C during catalysis will be discussed in the Results and Discussion, section 3.5 even though they were presented in Figure 2 along with those of Pd-CeO_2-air and Pd-CeO_2-H_2 before catalysis.

Different from Pd-CeO_2-air, the as-synthesized CeO_2 doped with Pd ions was pretreated in 5% H_2/Ar. It is termed Pd-CeO_2-H_2. Figure 3a is a TEM image of Pd-CeO_2-H_2 before catalysis. Unfortunately, Pd aggregated and formed some

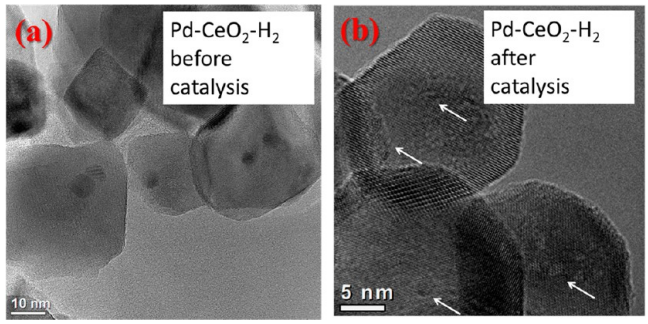

Figure 3. High-resolution TEM images of Pd-CeO_2-H_2 before (a) and after (b) catalysis. The arrows mark the nanoparticles in Pd-CeO_2-H_2 after the catalysis reaction. The average size of CeO_2 doped with Pd is 34.0 nm based on a statistical accounting of the nanoparticles in TEM images from different parts of the catalyst sample.

nanoparticles with a size of ~1–3 nm. Compared to the lack of metal nanoparticles in Pt-CeO_2-H_2 (Figure 8) and Rh-CeO_2-H_2 (Figure 13) upon pretreatment in H_2 at 500 °C, Pd in Pd-CeO_2-H_2 (Figure 3) forms Pd metal nanoparticles upon the same treatment. One potential reason for the formation of Pd nanoparticles in Pd-CeO_2 upon H_2 pretreatment could relate to the surface energy of metallic Pd nanoparticles, which is lower than that of Pt and Rh. It is reasonable to use the surface energies of the (111) faces of Pd, Pt, and Rh to represent the surface energies of their metal nanoparticles in general because of the lack of surface energy of the nanoparticles of these metals. Pd(111) has a surface energy of 1.88 J m^{-2} in contrast to 2.35 J m^{-2} of Pt (111) and 2.78 J m^{-2} of Rh(111).[65] The lower surface energy of Pd makes the formation of Pd metal nanoparticles relatively thermodynamically favorable in contrast to Pt and Rh. In addition, Pd can catalyze the dissociation of H_2 even at room temperature. Hydrogen atoms could further reduce other Pd ions to metal Pd atoms under a mild condition and even accelerate the nucleation to form Pd nanoparticles.

3.1.2. Catalytic Performance of Pd-CeO_2-air and Pd-CeO_2-H_2. Figure 4 presents the catalytic conversion and selectivity of Pd-CeO_2-air for MPO. The conversion of CH_4 increases as a function of temperature and reaches 84.0% at 700 °C (Table 1). Notably, the selectivity for the production of H_2 increases

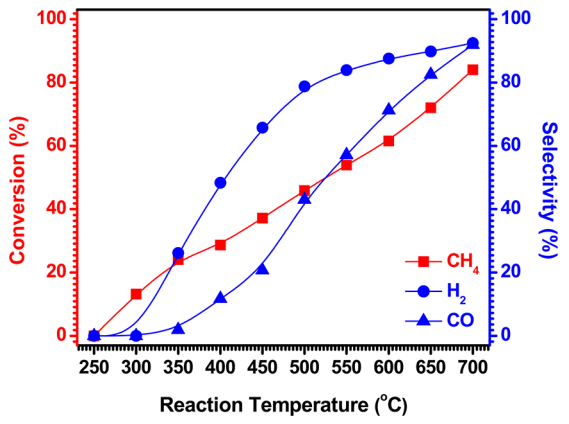

Figure 4. Catalytic performance of Pd-CeO_2-air. The left axis (red) and the red line show the conversion of methane. The right axis (blue) and the two blue lines show the selectivities for the production of H_2 (solid dot) and CO (solid triangle). S_{H2} (%) is defined as [moles of H_2 produced/(2 × moles of CH_4 consumed)] × 100. S_{CO} (%) is defined as [moles of CO produced/(moles of CH_4 consumed)] × 100.

dx.doi.org/10.1021/cs400070y | ACS Catal. 2013, 3, 2627–2639

Table 1. Catalytic Performance of Methane Partial Oxidation on Pd-CeO_2-air, Pt-CeO_2-air, and Rh-CeO_2-air catalysts[a]

temperature (°C)	catalyst	X_{CH4} (%)	S_{H2} (%)	S_{CO} (%)	H_2/CO ratio
300	Pd-CeO_2-air	13.2	0.0	0.0	
	Pt-CeO_2-air	1.8	0.0	0.0	
	Rh-CeO_2-air	5.3	0.0	0.0	
400	Pd-CeO_2-air	28.7	48.4	11.8	7.2
	Pt-CeO_2-air	28.8	44.8	5.8	14.7
	Rh-CeO_2-air	37.4	52.8	11.2	10.4
500	Pd-CeO_2-air	45.9	78.8	43.0	73.7
	Pt-CeO_2-air	43.9	72.2	36.6	4.2
	Rh-CeO_2-air	61.4	83.3	53.3	3.1
600	Pd-CeO_2-air	61.5	87.6	71.2	2.6
	Pt-CeO_2-air	53.1	74.2	56.6	2.6
	Rh-CeO_2-air	83.6	89.9	77.5	2.3
700	Pd-CeO_2-air	84.0	92.5	91.9	2.2
	Pt-CeO_2-air	74.6	88.5	85.8	2.3
	Rh-CeO_2-air	95.2	92.9	85.7	2.2

[a]The oxygen conversion was always 100%.

quickly in the temperature range of 300−500 °C. At 500 °C, it reaches 83% with a following increase to 92.5% at 700 °C. Compared to H_2, the selectivity of producing CO is less than that for H_2 by ~25−35% at a temperature lower than 500 °C. At temperatures higher than 500 °C, the difference in selectivity between CO and H_2 decreases. At 700 °C, it exhibits the same selectivity for the production of H_2 and CO. As shown in Figure 5, the ratio of H_2 to CO decreases with the temperature and reaches the stoichiometric ratio of 2 at a temperature higher than 500 °C.

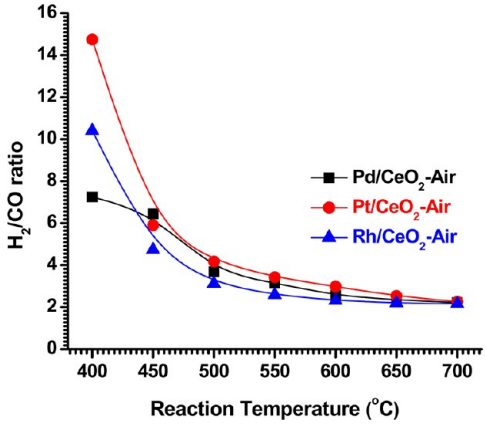

Figure 5. Molar ratio of H_2 to CO produced from MPO on Pd-CeO_2-air, Pt-CeO_2-air, and Rh-CeO_2-air in the temperature range of 400−700 °C.

In contrast to Pd-CeO_2-air, Pd-CeO_2-H_2 exhibits quite a different catalytic performance (Figure 6). There is no catalytic activity of MPO on Pd-CeO_2-H_2 at a temperature ≤500 °C. However, the conversion of CH_4 on Pd-CeO_2-H_2 rapidly increases in the temperature range of 550−700 °C (Figure 6a). This catalyst exhibits an evolution of the selectivity of H_2 that is very similar to that of CO (Figure 6b,c). In contrast to the sharp increase in both conversion and selectivity on Pd-CeO_2-H_2 at a temperature higher than 550 °C, Pd-CeO_2-air exhibits a progressive increase of activity and selectivity over the temperature range of 350−700 °C.

3.2. Pt-Doped CeO_2. *3.2.1. Pt-CeO_2-air and Pt-CeO_2-H_2 at Room Temperature.* Pt-doped CeO_2-air and Pt-doped CeO_2-H_2 were prepared with the same method as Pd-doped CeO_2-air and Pd-doped CeO_2-H_2, respectively. Figure 7a is one representative TEM image of the Pt-CeO_2-air before catalysis. TEM studies showed there are no nanoclusters identified, suggesting a homogeneous distribution of Pt ions in Pt-CeO_2-air before catalysis. A representative TEM image of Pt-CeO_2-air after catalysis is shown in Figure 7b. The lack of identifiable nanoparticles in Pt-CeO_2-air after catalysis suggests that there is not an aggregation of Pt atoms during catalysis. Figure 8a is a TEM image of Pt-CeO_2-H_2 before catalysis. Compared to Pd-CeO_2-H_2 before catalysis (Figure 3a), there are not any Pt nanoparticle identifiable in Pt-CeO_2-H_2 before catalysis (Figure 8a). In addition, the TEM image of Pt-CeO_2-H_2 after catalysis (Figure 8b) shows that there is no aggregation of Pt atoms during catalysis.

The deconvolution of the Pt 4f photoemission feature of Pt-CeO_2-air before catalysis (Figure 9a1) suggests that there could be three different types of Pt atoms, which each exhibit different bonding to oxygen atoms. There are also three different oxidation states of Pt atoms (Pt^0, Pt^{2+}, and Pt^{4+}) in Pt-CeO_2-H_2 before catalysis (Figure 9b1). It is noted that there are no Pt metal nanoparticles observed in the high-resolution TEM images even though there is a component with a binding energy of 71.2 eV in Pt-CeO_2-H_2 before catalysis. The lack of Pt metal nanoparticles is supported by detailed analysis of TEM and XPS. There were no Pt nanoparticles found in extensive studies of Pt-CeO_2-air and Pt-CeO_2-H_2. Alternatively, a Pt atom could bond to Ce atoms upon pretreatment in H_2. The removal of oxygen atoms bonding to Ce atoms could have created oxygen vacancies that a Pt atom nearby could fill in to form Pt−Ce bonds; in this case, Pt atoms do not form any Pt nanoparticles even though Pt exhibits a binding energy close to metallic Pt. We call this type of bonding of Pt the "pseudo-metallic state". The pseudo-metallic state of Pt will be further discussed in the Results and Discussion, section 3.5. In addition, a clear difference in the Ce 3d spectrum of Pt-CeO_2-air before catalysis (Figure 9c1) and Pt-CeO_2-H_2 before catalysis (Figure 9d1) is that the fraction of Ce^{3+} in Pt-CeO_2-H_2 before catalysis, 26%, is obviously larger than that in Pt-CeO_2-air before catalysis. The large density of oxygen vacancies could mean a large fraction of Pt atoms bonding to Ce atoms.

3.2.2. Catalytic Performance of Pt-CeO_2-air and Pt-CeO_2-H_2. The catalytic performances of Pt-CeO_2-air and Pt-CeO_2-H_2

dx.doi.org/10.1021/cs400070y | ACS Catal. 2013, 3, 2627−2639

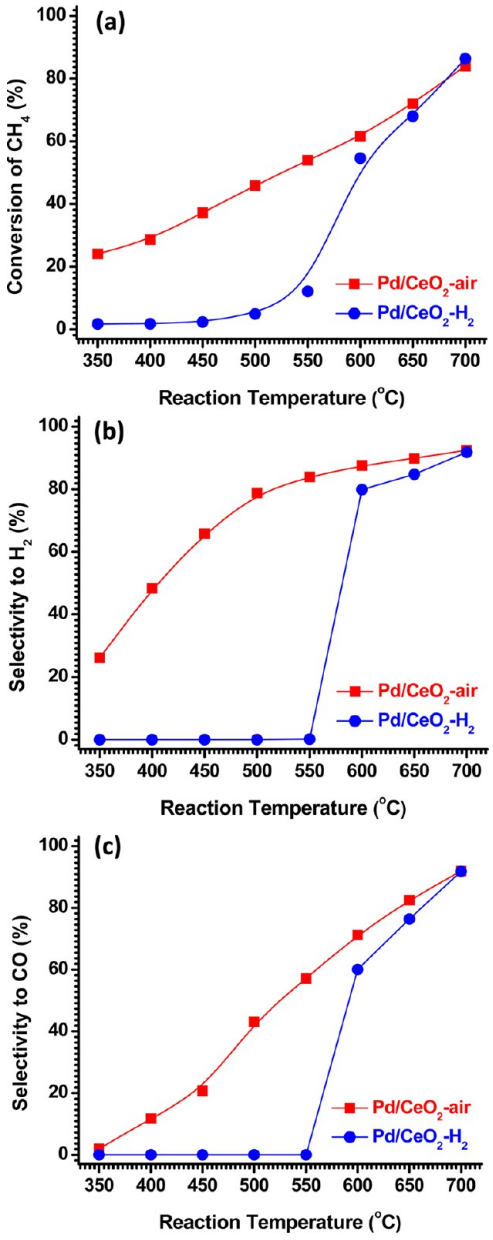

Figure 6. Catalytic performance of Pd-CeO_2-H_2 for MPO. Conversion of methane (a), selectivity to H_2 (b), and selectivity to CO (c). For the convenience of comparison, the catalytic performance of Pd-CeO_2-air (red line) under the same catalytic condition as Pd-CeO_2-H_2 (blue line) is listed in a parallel manner.

were measured. Figure 10 presents the catalytic conversion and selectivity for MPO on Pt-CeO_2-air. The conversion of CH_4 on Pt-CeO_2-air increases as a function of the reaction temperature and reaches 74.6% at 700 °C (Table 1). Notably, the selectivity for the production of H_2 increases rapidly in the temperature range of 300−500 °C. At 500 °C, it reaches 72.2%, with a following increase to 88.5% at 700 °C. Compared to the selectivity for H_2 production, the selectivity for the production of CO is lower by 10−20% at a temperature lower than 500 °C. At 700 °C, the selectivity for CO is the same as that for H_2 (Figure 10). Because of the higher H_2 selectivity of MPO on Pt-CeO_2-air at a low temperature such as 400 °C, the molar ratio of H_2 to CO at low temperatures (Figure 5) is much higher than the stoichiometric ratio of 2. The ratio of H_2 to CO in the

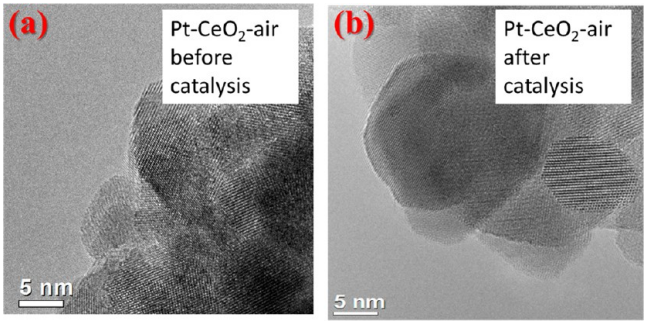

Figure 7. High-resolution TEM images of Pt-CeO_2-air before (a) and after (b) catalysis. The average size of CeO_2 doped with Pt is 9.5 nm based on a statistical accounting of the nanoparticles in the TEM images from different parts of the catalyst sample.

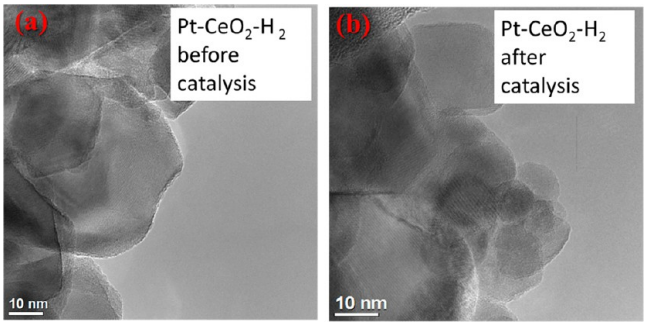

Figure 8. High-resolution TEM images of Pt-CeO_2-H_2 before (a) and after (b) catalysis. The average size of CeO_2 doped with Pt is 28.5 nm based on a statistical accounting of the nanoparticles in the TEM images from different parts of the catalyst sample.

temperature range of 400−500 °C (Figure 5) largely decreases. At a temperature higher than 500 °C, this ratio is further decreased to 2.

Compared to Pt-CeO_2-air, Pt-CeO_2-H_2 exhibits different catalytic performance. The conversion rate of CH_4 on Pt-CeO_2-H_2 gradually increases in the temperature range of 400−700 °C (Figure 11a). In addition, the conversion of CH_4 on Pt-CeO_2-H_2 is always lower than Pt-CeO_2-air by ∼15% up to 700 °C. In terms of selectivity for the production of H_2 and CO, Pt-CeO_2-H_2 is inferior to Pt-CeO_2-air throughout the whole temperature range (350−700 °C) (Figure 11b,c).

3.3. Rh-Doped CeO_2. *3.3.1. Rh-CeO_2-air and Rh-CeO_2-H_2 at Room Temperature.* Rh-CeO_2-air and Rh-CeO_2-H_2 were synthesized with the same method as those of Pt-CeO_2-air and Pt-CeO_2-H_2, respectively. The high-resolution TEM images in Figures 12 and 13 show that there are no nanoparticles in Rh-CeO_2-air before catalysis (Figure 12a), in Rh-CeO_2-air after catalysis (Figure 12b), in Rh-CeO_2-H_2 before catalysis (Figure 13a), and in Rh-CeO_2-H_2 after catalysis (Figure 13b). They further suggest that Rh ions were homogeneously distributed in CeO_2. Similar to Pd-CeO_2-H_2 before catalysis and Pt-CeO_2-H_2 before catalysis, the fraction of Ce^{3+} in the total Ce^{3+} and Ce^{4+} of Rh-CeO_2-H_2 before catalysis, 25%, is relatively high. In addition, the homogeneous doping of Rh ions in Rh-CeO_2-air before catalysis is supported by the lack of a Rh 3d photoemission feature of metallic Rh (Figure 14a1). Compared to Rh-CeO_2-air before catalysis, Rh in Rh-CeO_2-H_2 before catalysis is in a metallic state. However, there are no Rh nanoparticles observed in the TEM studies of Rh-CeO_2-H_2 before catalysis (Figure 13a). This pseudo-metallic state of Rh

dx.doi.org/10.1021/cs400070y | ACS Catal. 2013, 3, 2627−2639

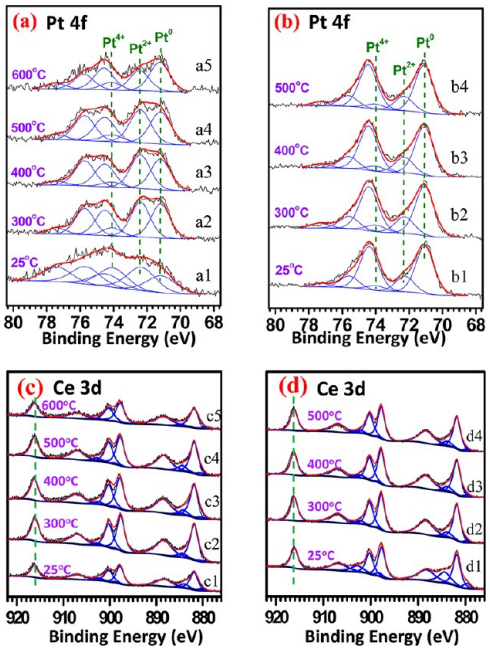

Figure 9. XPS spectra of the in situ studies of Pt 4f of Pt-CeO_2-air (a), Pt 4f of Pt-CeO_2-H_2 (b), Ce 3d of Pt-CeO_2-air (c), and Ce 3d of Pt-CeO_2-H_2 (d) during catalysis. The fwhm of the fitted peaks of Pt 4f in panels a and b were fixed at 1.2 eV, respectively. The ratio of the partial pressures of CH_4 to O_2 in the mixture reactant is 2:1. The flow rate is about 6 mL min^{-1}. All data were collected at the same pressure and flow rate of CH_4 and O_2. The only variable is the reaction temperature.

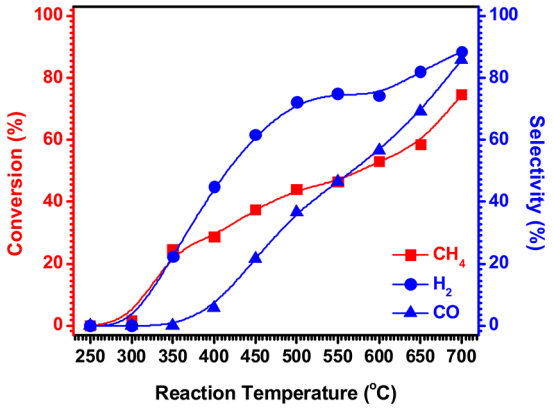

Figure 10. Catalytic performance of Pt-CeO_2-air. The left axis (red) and the red line show the conversion of methane. The right axis (blue) and the blue lines show the selectivities for the production of H_2 (solid dot) and CO (solid triangle).

in Rh-CeO_2-H_2 before catalysis can be rationalized with the two arguments made for Pt-CeO_2-air and Pt-CeO_2-H_2 in the Results and Discussion, section 3.2.1.

3.3.2. Catalytic Performance of Rh-CeO_2-air and Rh-CeO_2-H_2. The catalytic performance of Rh-CeO_2-air and Rh-CeO_2-H_2 was measured under the same conditions as the other catalysts. Figure 15 presents the catalytic conversion and selectivity of MPO on Rh-CeO_2-air. The conversion of CH_4 increases rapidly as a function of the reaction temperature and reaches 95.2% at 700 °C (Table 1). The selectivity for the production of H_2 increases fast in the temperature range of 300−500 °C (Figure 15). At 500 °C, it reaches 83.3% followed by a further increase to 92.9% at 700 °C. Compared to H_2 selectivity, the selectivity

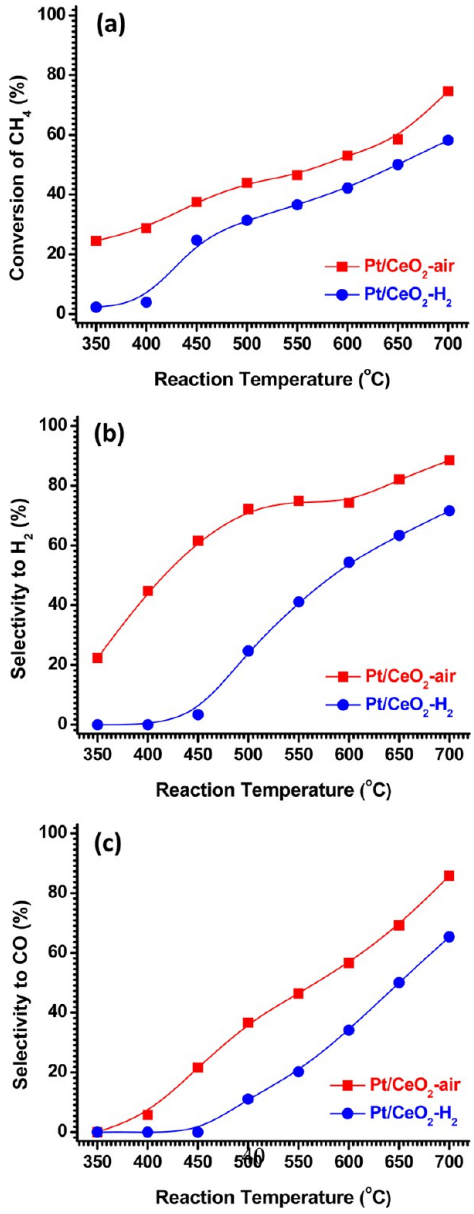

Figure 11. Catalytic performance of Pt-CeO_2-H_2. Conversion of methane (a), selectivity to H_2 (b), and selectivity to CO (c). For the convenience of comparison, the catalytic performance of Pt-CeO_2-air (red line) under the same catalytic condition as Pt-CeO_2-H_2 (blue line) is listed in a parallel manner.

for CO is less than that for H_2 by 20−30% at a temperature lower than 500 °C. As shown in Figure 5, the H_2-to-CO ratio in the temperature range of 400−500 °C is far greater than 2; at temperatures higher than 500 °C, the ratio is decreased to 2.

As shown in Figure 16, Rh-CeO_2-H_2 exhibits a catalytic performance almost identical to Rh-CeO_2-air in the temperature range of 350−700 °C. This is different from the obvious variation between Pt-CeO_2-air and Pt-CeO_2-H_2 (Figure 11) and that between Pd-CeO_2-air and Pd-CeO_2-H_2 (Figure 6). In addition, among Pd-CeO_2-air, Pd-CeO_2-H_2, Pt-CeO_2-air, Pt-CeO_2-H_2, Rh-CeO_2-air, and Rh-CeO_2-H_2, the difference in catalytic conversion and selectivity to CO and H_2 between Pd-CeO_2-air and Pd-CeO_2-H_2 is much larger than those between Pt-CeO_2-air and Pt-CeO_2-H_2 and between Rh-CeO_2-air and Rh-CeO_2-H_2. In the case of Pd-CeO_2-H_2, this could result from

dx.doi.org/10.1021/cs400070y | ACS Catal. 2013, 3, 2627−2639

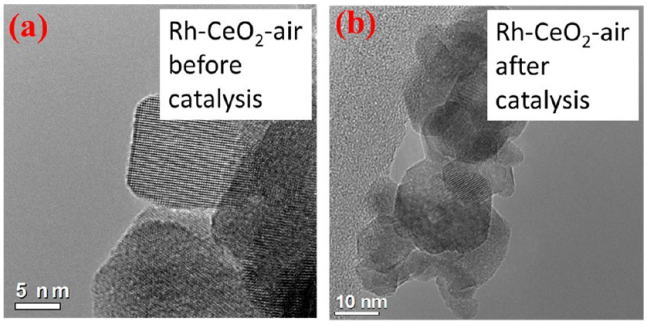

Figure 12. High-resolution TEM images of Rh-CeO_2-air before (a) and after (b) catalysis. The average size of CeO_2 doped with Rh is 22.5 nm based on a statistical accounting of the nanoparticles in the TEM images from different parts of the catalyst sample.

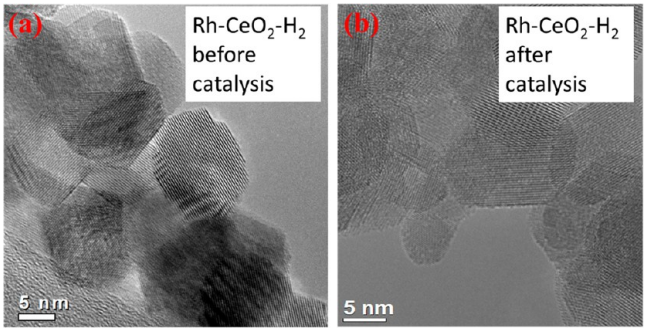

Figure 13. High-resolution TEM images of Rh-CeO_2-H_2 before (a) and after (b) catalysis. The average size of CeO_2 doped with Rh is 30.5 nm based on a statistical accounting of the nanoparticles in the TEM images from different parts of the catalyst sample.

some side reactions on the Pd metal nanoparticles. At 700 °C, Rh-CeO_2-air and Rh-CeO_2-H_2 have a similar selectivity for H_2 and CO of 88−94%, respectively (Figure 16). At this temperature, the ratio of H_2 to CO is the stoichiometric ratio, 2.

3.4. Turnover Frequency and Apparent Activation Energy. For a parallel comparison of the catalytic performances in a kinetics-controlled regime, turnover frequencies (TOF) and apparent activation energy (E_a) for MPO on the six catalysts were measured. In all of these measurements, the highest conversion of CH_4 remained less than 15%. Because Pd metal nanoparticles were clearly observed in Pd-CeO_2-H_2 after catalysis (Figure 3b), we did not calculate the TOF of Pd-CeO_2-H_2. For the other five catalysts (Pd-CeO_2-air, Pt-CeO_2-air, Pt-CeO_2-H_2, Rh-CeO_2-air, and Rh-CeO_2-H_2), we experimentally evaluated their TOFs under the assumption that all atoms of Pd, Pt, or Rh on the surface layers of the five catalysts are active sites for MPO regardless of whether they appear in a metallic or ionic state. In the Results and Discussion, section 3.5, we rationalize that the pseudo-metallic state of Pd in Pd-CeO_2-air and of Pt in Pt-CeO_2-H_2 and Pt-CeO_2-air observed during catalysis are not metal atoms of metal nanoparticles. The ratios of the noble metal (Pd, Pt, or Rh) of the topmost surface layer to Ce of the topmost surface layer during catalysis at different temperatures were calculated using the peak areas of Pd 3d, Pt 4f, Rh 3d, and Ce 3d collected during catalysis through Beer's law. The calculated atomic ratios of Pd, Pt, and Rh to Ce during catalysis are listed in Figure S4. They are approximately close to the bulk ratios of doped ions in CeO_2. The procedure of calculating TOFs is also described in the

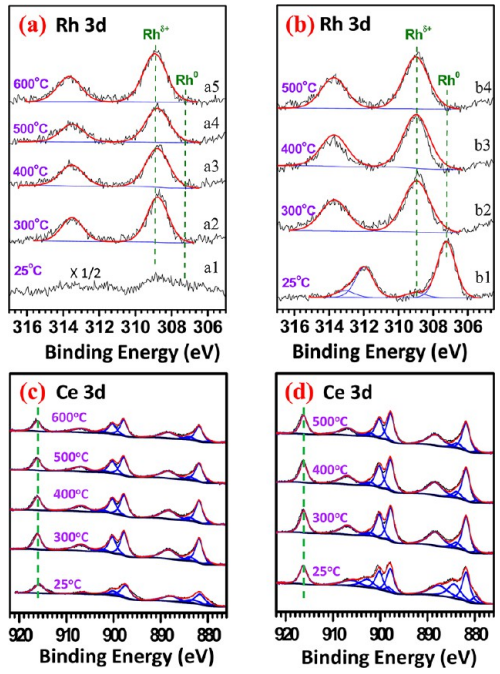

Figure 14. XPS spectra of the in situ studies of Rh 3d of Rh-CeO_2-air (a), Rh 3d of Rh-CeO_2-H_2 (b), Ce 3d of Rh-CeO_2-air (c), and Ce 3d of Rh-CeO_2-H_2 (d) during catalysis. The fwhm of the fitted peaks of Rh 3d in panels a and b were constrained between 1.2 and 1.4 eV, respectively. The ratio of the partial pressures of CH_4 to O_2 in the mixture reactant is 2:1, with a total pressure of 3 Torr. The flow rate is 6 mL/min. All AP−XPS data were collected at the same pressure and flow rate of CH_4 and O_2. The only variable is the reaction temperature.

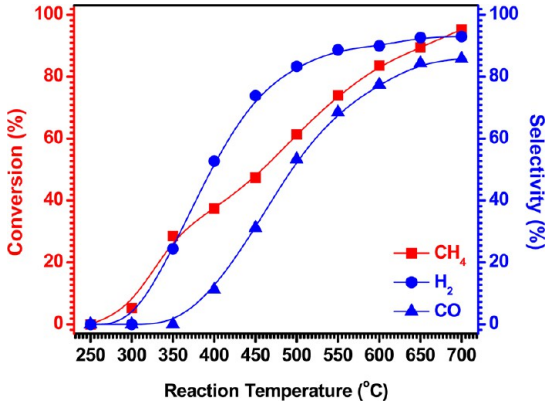

Figure 15. Catalytic performance of Rh-CeO_2-air. The left axis (red) and the red line show the conversion of methane. The right axis (blue) and the blue lines show the selectivities to the production of H_2 (solid dot) and CO (solid triangle).

Supporting Information. The calculated TOF at different temperatures is plotted in Figure 17. Obviously, Rh-doped catalysts (Rh-CeO_2-H_2 and Rh-CeO_2-air) exhibit catalytic activity higher than Pt- and Pd-doped catalysts (Pd-CeO_2-air, Pt-CeO_2-H_2, and Pt-CeO_2-air). In addition, they also exhibit higher catalytic selectivity for the production of CO and H_2 than Pd- and Pt-doped catalysts based on the catalytic performances presented in Figures 4−6, 10, 11, 15, and 16.

The measurements of the apparent activation energy, E_a, for the six catalysts were performed by controlling the catalytic conversion of CH_4 to be lower than 15%. Figure 18 is the Arrhenius plots of MPO on the six catalysts at different

dx.doi.org/10.1021/cs400070y | ACS Catal. 2013, 3, 2627−2639

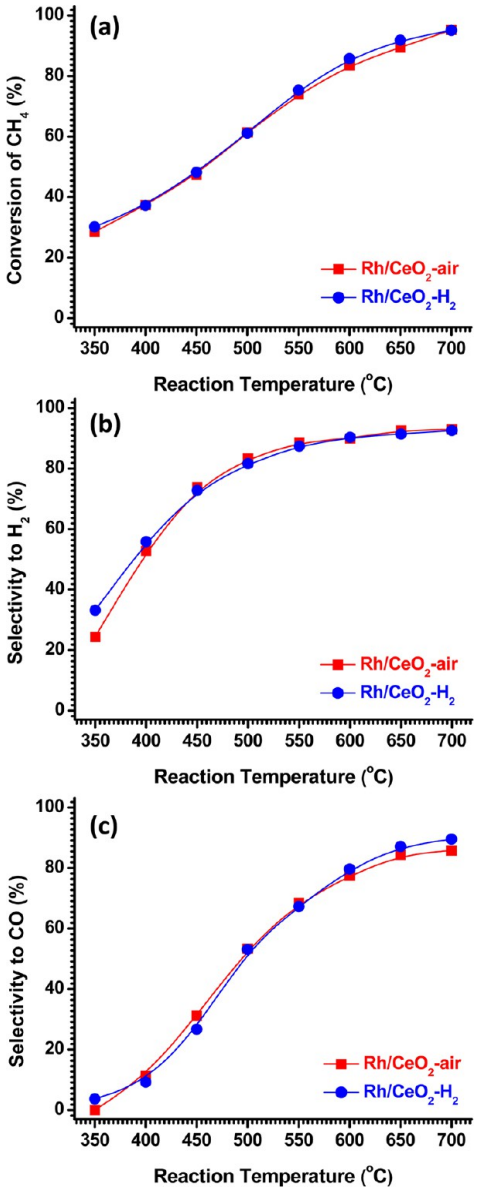

Figure 16. Catalytic performance of Rh-CeO_2-H_2. Conversion of methane (a), selectivity to H_2 (b), and selectivity to CO (c). For the convenience of comparison, the catalytic performance of Rh-CeO_2-air (red line) under the same catalytic condition as Rh-CeO_2-H_2 (blue line) is listed in a parallel manner.

temperature ranges. In these plots, the variable is the conversion rate of CH_4. Thus, the calculated activation energies from the slopes of these plots (Figure 18) are only the apparent activation energies. For Pt-CeO_2-air, Pd-CeO_2-air, Rh-CeO_2-air, and Rh-CeO_2-H_2, the measurements of E_a were conducted in the temperature range of 360−410 °C. Among them, Pd-CeO_2-air and Pt-CeO_2-air have rather high apparent activation barriers of 204.9 and 338.0 kJ mol^{-1}, respectively (Figure 18) in this temperature region. These quite high activation energies could result from the coexistence of both oxidizing and metallic Pt and Pd atoms in Pd-CeO_2-air and Pt-CeO_2-air, which offset the measured E_a. Rh-CeO_2-air has a much lower activation energy of 30.2 kJ mol^{-1} in contrast to Pd-CeO_2-air and Pt-CeO_2-air. The active phase of Rh-CeO_2-air is CeO_2 doped with Rh^{n+} ions. It is worth noting that Rh-CeO_2-H_2 exhibits an activation barrier very similar to Rh-CeO_2-air, consistent with

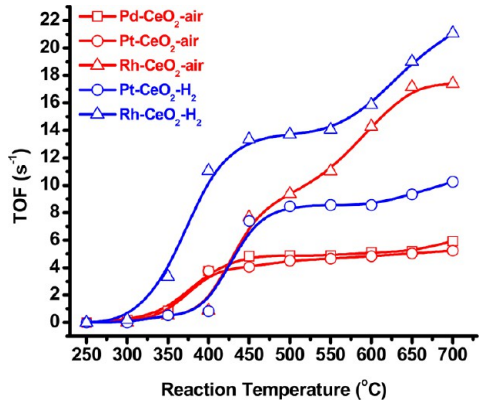

Figure 17. Turnover frequency of MPO on Rh-CeO_2-H_2, Rh-CeO_2-air, Pd-CeO_2-H_2, Pd-CeO_2-air, Pt-CeO_2-H_2, and Pt-CeO_2-air measured in a kinetics-controlled regime.

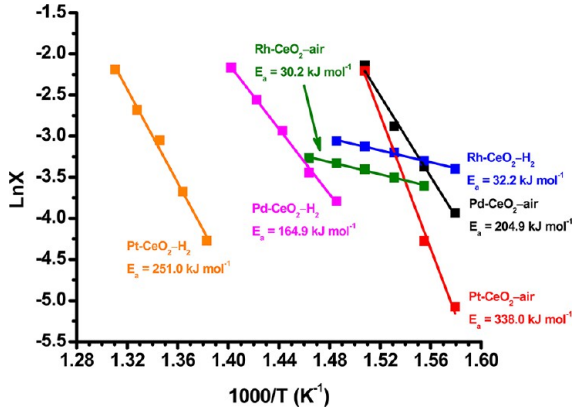

Figure 18. Arrhenius plots of MPO on catalysts Rh-CeO_2-H_2, Rh-CeO_2-air, Pd-CeO_2-H_2, Pd-CeO_2-air, Pt-CeO_2-H_2, and Pt-CeO_2-air. In LnX, X is the conversion rate.

the identity of the surface chemistry of the two catalysts during catalysis (Figure 14).

3.5. In Situ AP−XPS Studies and Correlation to Catalytic Performance. To understand the different catalytic behaviors of these catalysts, in situ studies of the surface chemistries of these catalysts during catalysis were performed with our in-house ambient-pressure XPS. Photoelectrons were excited with a monochromatic Al Kα source for a better resolution. In situ AP−XPS studies of the six catalysts were performed at a temperature up to 600 °C for M-CeO_2-air or 500 °C for M-CeO_2-H_2. The collected spectra have a good signal-to-noise ratio. A continuous accumulation of atomic carbon that dissociated from CH_4 at high temperatures blocked the nozzle between the reaction cell and the energy analyzer and thus prevented it from collecting photoelectrons during in situ studies of Pd-CeO_2-H_2, Pt-CeO_2-H_2, and Rh-CeO_2-H_2 at 600 °C and higher. The temperature of the aperture must have been very high because the distance between the sample surface and the aperture is only 1 mm or less. Thus, we have to limit the highest temperature for taking spectra during catalysis of Pd-CeO_2-H_2, Pt-CeO_2-H_2, and Rh-CeO_2-H_2 to 500 °C (Figures 2b, 9b, and 14b).

Figure 14 presents the photoemission features of Rh 3d of Rh-CeO_2-air and Rh-CeO_2-H_2 at catalytic temperatures in a mixture of 2 Torr CH_4 and 1 Torr O_2. For Rh-CeO_2-air during catalysis (Figure 14a2−a5), Rh is in an oxidizing state in the

dx.doi.org/10.1021/cs400070y | ACS Catal. 2013, 3, 2627−2639

temperature range of 300−500 °C. TEM studies of Rh-CeO_2-air and Rh-CeO_2-H_2 after catalysis suggested that there are no Rh or RhO_x nanoparticles on or in CeO_2 (Figures 12b and 13b). These experimental data from in situ studies showed the preservation of an ionic state of Rh in Rh-CeO_2-air before catalysis, during catalysis, and after catalysis. The preservation of an ionic state of Rh of Rh-CeO_2-air during catalysis can be rationalized by the high bond strength of Rh−O bonds.[50]

In contrast to Rh-CeO_2-air, Rh in Rh-CeO_2-H_2 before catalysis (Figure 14b1) is in a metallic state in the surface region. However, the TEM studies of the catalyst, Rh-CeO_2-H_2 before catalysis, showed there are no Rh metal nanoparticles. In fact, the high density of oxygen vacancies in catalyst Rh-CeO_2-H_2 before catalysis (Figure 14d1) supports that Rh likely bonds to Ce atoms upon the removal of some of the surface lattice oxygen atoms of CeO_2. The direct bonding of a Rh atom to Ce atoms makes Rh appear to be in a metallic state although there are no Rh nanoparticles formed. Here, we call the low binding energy of Rh 3d of Rh bonding to Ce atoms a pseudo-metallic state because the Rh atoms do not form any Rh metal nanoparticles.

AP−XPS studies showed that Rh of Rh-CeO_2-H_2 was oxidized to an ionic state during catalysis at 300 °C (Figure 14b2). TEM studies of Rh-CeO_2-H_2 after catalysis (Figure 13b) showed there are no RhO_x nanoparticles. The upshift in Rh 3d was driven by the oxidization of Rh atoms bonding to Ce atoms (in an pseudo-metallic state) in an ionic state in the reactant mixture (CH_4 and O_2) during catalysis. The similarity in surface chemistry (Figure 14a4,b4) of Rh-CeO_2-air and Rh-CeO_2-H_2 during catalysis is consistent with the similarity in their catalytic performance (Figure 16).

In situ AP−XPS showed that the surface chemistries of Pt-CeO_2-H_2 and Pt-CeO_2-air during catalysis are different even though the catalytic conditions are exactly the same. In the case of Pt-CeO_2-H_2, 76% Pt atoms remain in a pseudo-metallic state in the temperature range of 300−500 °C during catalysis (Figure 9b). However, about 52% ionic Pt of Pt-CeO_2-air is reduced to a pseudo-metallic state during catalysis (Figure 9a). Compared to the preservation of the ionic state of Rh of Rh-CeO_2-air during catalysis, the reduction of the ionic state Pt of Pt-CeO_2-air to a pseudo-metallic state during catalysis results from the low bond strength of Pt−O. Rh−O bonds have a larger formation energy than Pt−O.[66,67]

Through correlating the surface chemistries of Pt-CeO_2-air and Pt-CeO_2-H_2 during catalysis to the corresponding catalytic performances, we deduce that the high conversion of methane on Pt-CeO_2-air (Figure 11a) could result from the high fraction of Pt ions in Pt-CeO_2-air compared to Pt-CeO_2-H_2 during catalysis (Figure 9). This is consistent with the understanding of the catalytic performance on CeO_2 doped with Pt for MPO based on DFT calculation.[47] The DFT calculation[47] showed that the ionic-state Pt doped in the lattice of CeO_2 can decrease the bond strength of surface-lattice oxygen to Ce ions, which further decreases the activation barrier for breaking C−H on the surface-lattice oxygen atoms.[47]

In the catalysis of MPO on Pt-CeO_2-air, Pt-CeO_2-H_2, Pd-CeO_2-air, and Pd-CeO_2-H_2, the ratio of H_2 to CO is always higher than the stoichiometric ratio of MPO, 2, at a temperature lower than 650−700 °C (Figure 5). This means that the selectivity for the production of CO on these catalysts is always lower than that of H_2 at a temperature lower than 650−700 °C. This is probably related to a side reaction, a water-gas shift (WGS) performed at the metal-oxide interface,[68] because Pt or Pd in a pseudo-metallic state are formed based on the in situ AP−XPS studies. WGS consumes CO and H_2O to produce CO_2 and H_2. A high reaction temperature is not favorable for the conversion because WGS is slightly exothermic. However, at a relatively low temperature, some CO and H_2O are converted to CO_2 and H_2 through WGS because H_2O is formed during the combustion of CH_4. The WGS at a relatively low temperature increased the overall selectivity for the production of H_2, leading to a higher ratio of H_2 to CO at a relatively low temperature. At a high temperature, the WGS is not thermodynamically favorable; thus, the influence of WGS on the ratio of H_2 to CO is negligible, and the ratio of H_2 to CO decreases to the stoichiometric ratio of MPO, 2:1, at high temperatures, such as 700 °C.

The high ratio of H_2 to CO of MPO on Rh-CeO_2-air and Rh-CeO_2-H_2 cannot be rationalized with the above argument. This is because Rh is in an ionic state during MPO. There are no sites for WGS. Alternatively, the high ratio of H_2 to CO in MPO on Rh-CeO_2-air and Rh-CeO_2-H_2 could result from a different side reaction, CO oxidation. By considering the reported high activity of CO oxidation on a RhO_x thin film formed on Rh nanoparticles,[69,70] the Rh-ions-doped oxide surface may catalyze CO oxidation with a low activation energy. CO oxidation on Rh-CeO_2-air and Rh-CeO_2-H_2 can consume CO and thus increase the H_2/CO ratio. A computational study was suggested to provide insights for the expected activity of CO oxidation on this Rh^{n+}-doped oxide surface.

Compared to Rh-CeO_2-H_2, Rh-CeO_2-air, Pt-CeO_2-H_2, and Pt-CeO_2-air, the evolution of the surface chemistries of Pd-CeO_2-H_2 and Pd-CeO_2-air are more complicated. As shown in Figure 2a1,b1, the surface chemistries of Pd-CeO_2-air and Pd-CeO_2-H_2 before catalysis are quite different. Pd exhibits an oxidizing state in Pd-CeO_2-air before catalysis in contrast to Pd-CeO_2-H_2 before catalysis in which the majority of Pd is in the metallic state (Figure 2d1). This is supported by the observation of Pd metal nanoparticles in the TEM studies. In situ studies using AP−XPS showed that ionic Pd of Pd-CeO_2-air is partially reduced to metallic Pd during catalysis and the fraction of metallic Pd nanoparticles of Pd-CeO_2-air increases with the rising reaction temperature in the temperature range of 300−600 °C (Figure 2a). This is partially due to the reduction of the doped Pd ions by the products of MPO, H_2, and/or CO. All Pd in the Pd-CeO_2-air during catalysis at 600 °C exists in a pseudo-metallic state (Figure 2a5) because there are no Pd metal nanoparticles observed in the Pd-CeO_2-air after catalysis (Figure 1b). Correspondingly, Pd-CeO_2-air at 600 °C exhibits a high conversion and selectivity for the production of H_2 and CO (Figure 4). Correlations of the surface chemistries during catalysis and the corresponding catalytic performances show that the pseudo-metallic state of Pd is a component of an active site.

Figure 2b1−b4 suggest that the Pd metal nanoparticles of Pd-CeO_2-H_2 before catalysis were oxidized during catalysis. This is quite different from the partial reduction of the doped Pd ions of Pd-CeO_2-air during catalysis. In fact, this difference can be rationalized by their catalytic activity. As shown in Figure 6a, Pd-CeO_2-H_2 is active for MPO only at a temperature higher than 500 °C. At a temperature ≤500 °C, the reactive environment is a mixture of CH_4 and O_2 without any component of a reducing gas such as CO or H_2. Certainly, O_2 readily oxidized the Pd metal nanoparticles of Pd-CeO_2-H_2 during catalysis to ionic Pd (Figures 2b1−b4). As the oxidation

dx.doi.org/10.1021/cs400070y | ACS Catal. 2013, 3, 2627−2639

of Pd metal nanoparticles must be performed on the external surface of Pd nanoparticles, a core−shell structured Pd@PdO_x was formed in the temperature range of 300−500 °C (Figures 2b2−b4). The lack of activity of Pd@PdO_x at 300−500 °C suggests that the PdO_x shell is not active for MPO. It is noted that the coordination environment of Pd ions of the PdO_x shell formed through oxidation of the Pd layer of Pd metal plates is different from that of Pt ions or Rh ions doped in the lattice of CeO_2. The Pd ions doped in the lattice of CeO_2 likely activate neighboring oxygen atoms of CeO_2 and thus decrease the activation energy of C−H dissociation on oxygen atoms of the surface lattice. However, Pd ions of PdO_x formed on Pd-CeO_2-H_2 in the mixture of CH_4 and O_2 (Figure 2b) cannot activate oxygen atoms of CeO_2 because Pd ions in this case are in a PdO_x shell of a Pd@PdO_x nanoparticle instead of the surface lattice of CeO_2. Thus, the PdO_x shell formed on Pd-CeO_2-H_2 in the temperature range of 300−500 °C in the mixture of CH_4 and O_2 is not active for MPO. Thus far, we have developed the correlations of the in situ surface chemistries of the six catalysts during catalysis and their corresponding catalytic performances.

Because Pd-CeO_2-air, Pt-CeO_2-air, and Rh-CeO_2-air exhibit better catalytic performance than Pd-CeO_2-H_2, Pt-CeO_2-H_2, and Rh-CeO_2-H_2, respectively, we performed tests of stability of MPO on Pd-CeO_2-air, Pt-CeO_2-air, and Rh-CeO_2-air at 600 °C. As shown in Figure 19, the catalytic performances of the three catalysts, including conversion, selectivity to H_2 and CO, and the ratio of H_2 to CO, remain nearly constant in the first 24 h.

4. CONCLUSIONS

Pd-CeO_2-air, Pd-CeO_2-H_2, Pt-CeO_2-air, Pt-CeO_2-H_2, Rh-CeO_2-air, and Rh-CeO_2-H_2 catalysts were synthesized. Pd, Pt, and Rh ions were successfully doped into CeO_2 in Pd-CeO_2-air, Pt-CeO_2-air, Pt-CeO_2-H_2, Rh-CeO_2-air, and Rh-CeO_2-H_2, although Pd metal nanoparticles were formed on CeO_2 of Pd-CeO_2-H_2 before catalysis. These well-controlled, parallel studies of the six different catalysts (Pd-CeO_2-air, Pd-CeO_2-H_2, Pt-CeO_2-air, Pt-CeO_2-H_2, Rh-CeO_2-air, and Rh-CeO_2-H_2) revealed quite different catalytic performances even though they were synthesized with the same method. Pd-CeO_2-air exhibits higher catalytic activity than Pd-CeO_2-H_2 in the temperature range of 300−550 °C. In situ studies of the surface chemistry of the catalysts suggested that the pseudo-metallic state of Pd is active for MPO. For Pt-CeO_2-H_2, Pt ions were partially reduced. A comparative study of Pt-CeO_2-air and Pt-CeO_2-H_2 during catalysis suggests that Pt ions doped in the surface lattice of CeO_2 are a component of the active sites of MPO. Compared to Pd-CeO_2-air, Pd-CeO_2-H_2, Pt-CeO_2-air, and Pt-CeO_2-H_2, Rh in Rh-CeO_2-air and Rh-CeO_2-H_2 always remains in an ionic state. Clearly, Rh ions doped in the CeO_2 lattice are a component of the active sites.

Overall, we developed correlations between the evolution of catalytic performances of the six catalysts and their corresponding surface chemistries at different temperatures through in situ studies of the surface chemistry of the six CeO_2-based catalysts. These correlations between the experimental evaluations of catalytic performances and the corresponding surface chemistries during catalysis suggest the necessity of in situ studies in understanding catalysis. Without in situ studies of surface chemistry of catalysts during catalysis, the different surface chemistries of Rh-CeO_2-air and Rh-CeO_2-H_2 before catalysis (Figure 14a1,b1) identified with ex situ studies contradict the same catalytic performance of MPO on Rh-CeO_2-air and Rh-CeO_2-H_2 during catalysis.

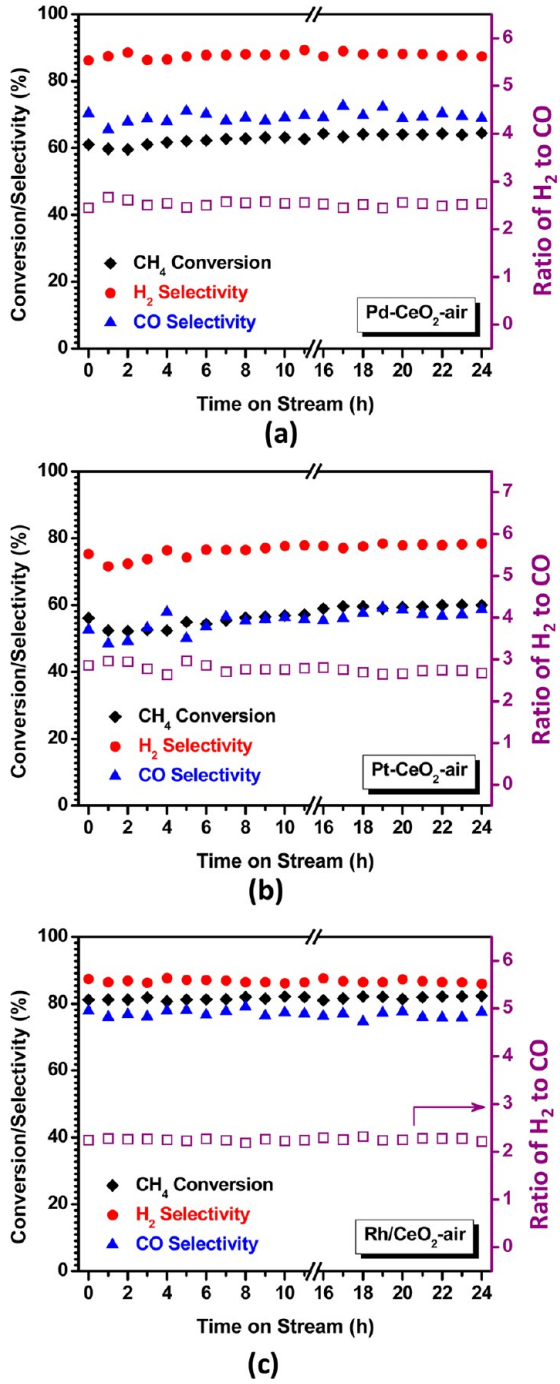

Figure 19. Stability tests of conversion, selectivity, and ratio of H_2 to CO of Pd-CeO_2-air (a), Pt-CeO_2-air (b), and Rh-CeO_2-air (c) at 600 °C.

■ ASSOCIATED CONTENT

Supporting Information

Schematic showing gas flow and heating in the catalysis reactor integrated in the APXPS system; catalytic performance of pure CeO_2 for methane partial oxidation; XRD patterns of catalysts after catalysis; atomic ratio of Pd, Pt, or Rh in the topmost surface layer to Ce of the topmost surface layer of the catalysts during catalysis; and calculation of turn-over frequency. This

dx.doi.org/10.1021/cs400070y | ACS Catal. 2013, 3, 2627−2639

material is available free of charge via the Internet at http://pubs.acs.org.

AUTHOR INFORMATION

Corresponding Author

*E-mail: ftao@nd.edu. Tel.: (+1) 574 631 1394.

Author Contributions

†These authors equally contributed to this work.

Notes

The authors declare no competing financial interest.

ACKNOWLEDGMENTS

This work is partially supported by the Chemical Sciences, Geosciences and Biosciences Division, Office of Basic Energy Sciences, Office of Science, U.S. Department of Energy, under the Grant DE-FG02-12ER1635.

REFERENCES

(1) Goetsch, D. A.; Schmidt, L. D. *Science* **1996**, *271*, 1560−1562.
(2) Wilson, J. N.; Pedigo, R. A.; Zaera, F. *J. Am. Chem. Soc.* **2008**, *130*, 15796−15797.
(3) Donazzi, A.; Livio, D.; Maestri, M.; Beretta, A.; Groppi, G.; Tronconi, E.; Forzatti, P. *Angew. Chem., Int. Ed.* **2011**, *50*, 3943−3946.
(4) Nagaoka, K.; Sato, K.; Takita, Y. *J. Catal.* **2012**, *287*, 86−92.
(5) Tsang, S. C.; Claridge, J. B.; Green, M. L. H. *Catal. Today* **1995**, *23*, 3−15.
(6) Pena, M. A.; Gomez, J. P.; Fierro, J. L. G. *Appl. Catal., A* **1996**, *144*, 7−57.
(7) Sokolovskii, V. D.; Coville, N. J.; Parmaliana, A.; Eskendirov, I.; Makoa, M. *Catal. Today* **1998**, *1998*, 191−195.
(8) Rostrup-Nielsen, J. R. *Catal. Today* **2002**, *71*, 243−247.
(9) York, A. P. E.; Xiao, T.; Green, M. L. H. *Top. Catal.* **2003**, *22*, 345−358.
(10) York, A. P. E.; Xiao, T.-C.; Green, M. L. H.; Claridge, J. B. *Catal. Rev.* **2007**, *49*, 511−560.
(11) Christian Enger, B.; Lødeng, R.; Holmen, A. *Appl. Catal., A* **2008**, *346*, 1−27.
(12) Choudhary, T. V.; Choudhary, V. R. *Angew. Chem., Int. Ed.* **2008**, *47*, 1828−1847.
(13) Otsuka, K.; Ushiyama, T.; Yamanaka, I. *Chem. Lett.* **1993**, 1517−1520.
(14) Otsuka, K.; Wang, Y.; Sunada, E.; Yamanaka, I. *J. Catal.* **1998**, *175*, 152−160.
(15) Au, C.-T.; Ng, C.-F.; Liao, M.-S. *J. Catal.* **1999**, *185*, 12−22.
(16) Ruckenstein, E.; Wang, H. Y. *J. Catal.* **1999**, *187*, 151−159.
(17) Ruckenstein, E. *J. Catal.* **2000**, *190*, 32−38.
(18) Basile, F.; Fornasari, G.; Gazzano, M.; Vaccari, A. *J. Mater. Chem.* **2002**, *12*, 3296−3303.
(19) Horn, R.; Williams, K.; Degenstein, N.; Schmidt, L. *J. Catal.* **2006**, *242*, 92−102.
(20) Eriksson, S.; Rojas, S.; Boutonnet, M.; Fierro, J. L. G. *Appl. Catal., A* **2007**, *326*, 8−16.
(21) Montini, T.; Condò, A. M.; Hickey, N.; Lovey, F. C.; De Rogatis, L.; Fornasiero, P.; Graziani, M. *Appl. Catal., B* **2007**, *73*, 84−97.
(22) Bitsch-Larsen, A.; Degenstein, N. J.; Schmidt, L. D. *Appl. Catal., B* **2008**, *78*, 364−370.
(23) Bitsch-Larsen, A.; Horn, R.; Schmidt, L. D. *Appl. Catal., A* **2008**, *348*, 165−172.
(24) Donazzi, A.; Michael, B. C.; Schmidt, L. D. *J. Catal.* **2008**, *260*, 270−275.
(25) Michael, B. C.; Donazzi, A.; Schmidt, L. D. *J. Catal.* **2009**, *265*, 117−129.
(26) Tanaka, H.; Kaino, R.; Okumura, K.; Kizuka, T.; Tomishige, K. *J. Catal.* **2009**, *268*, 1−8.
(27) Basile, F.; Benito, P.; Fornasari, G.; Monti, M.; Scavetta, E.; Tonelli, D.; Vaccari, A. *Catal. Today* **2010**, *157*, 183−190.
(28) Karelovic, A.; García, X.; Wojcieszak, R.; Ruiz, P.; Gordon, A. L. *Appl. Catal., A* **2010**, *384*, 220−229.
(29) Tanaka, H.; Kaino, R.; Nakagawa, Y.; Tomishige, K. *Appl. Catal., A* **2010**, *378*, 187−194.
(30) Tanaka, H.; Kaino, R.; Okumura, K.; Kizuka, T.; Nakagawa, Y.; Tomishige, K. *Appl. Catal., A* **2010**, *378*, 175−186.
(31) Boullosa-Eiras, S.; Zhao, T.; Vanhaecke, E.; Chen, D.; Holmen, A. *Catal. Today* **2011**, *178*, 12−24.
(32) Mateos-Pedrero, C.; Duquesne, S.; Carrazán, S. R. G.; Soria, M. A.; Ruíz, P. *Appl. Catal., A* **2011**, *394*, 245−256.
(33) Berger-Karin, C.; Wohlrab, S.; Rodemerck, U.; Kondratenko, E. V. *Catal. Commun.* **2012**, *18*, 121−125.
(34) Liander, H. *Trans. Faraday Soc.* **1929**, *25*, 462.
(35) Ashcroft, A. T.; Cheetham, A. K.; Foord, J. S.; Green, M. L. H.; Grey, C. P.; Murrell, A. J.; Vernon, P. D. F. *Nature* **1990**, *344*, 319−321.
(36) Hargreaves, J. S. J.; Hutchings, G. J.; Joyner, R. W. *Nature* **1990**, *348*, 428−429.
(37) Choudhary, V. R.; Mamman, A. S.; Sansare, S. D. *Angew. Chem., Int. Ed. Engl.* **1992**, *31*, 1189−1190.
(38) Hickman, D. A.; Schmidt, L. D. *Science* **1993**, *259*, 343−347.
(39) Ashcroft, A. T.; Cheetham, A. K.; Green, M. L. H.; Vernon, P. D. F. *Nature* **1991**, *352*, 225−226.
(40) Pino, L.; Vita, A.; Cordaro, M.; Recupero, V.; Hegde, M. S. *Appl. Catal., A* **2003**, *243*, 135−146.
(41) Pantu, P.; Gavalas, G. R. *Appl. Catal., A* **2002**, *223*, 253−260.
(42) Pino, L.; Recupero, V.; Beninati, S.; Shukla, A. K.; Hegde, M. S.; Bera, P. *Appl. Catal., A* **2002**, *225*, 63−75.
(43) Souza, M. M. V. M; Schmal, M. *Catal. Lett.* **2003**, *91*, 11−17.
(44) Passos, F. B.; de Oliveira, E. R.; Mattos, L. V.; Noronha, F. B. *Catal. Today* **2005**, *101*, 23−30.
(45) Passos, F. B.; Oliveira, E. R.; Mattos, L. V.; Noronhe, F. B. *Catal. Lett.* **2006**, *110*, 261−267.
(46) Ahn, K.; Chung, Y.-C.; Oh, J. H.; Hari Prasad, D.; Kim, H.; Kim, H.-R.; Son, J.-W.; Lee, H.-W.; Lee, J.-H. *J. Nanosci. Nanotechnol.* **2011**, *11*, 6414−6419.
(47) Tang, W.; Hu, Z.; Wang, M.; Stucky, G. D.; Metiu, H.; McFarland, E. W. *J. Catal.* **2010**, *273*, 125−137.
(48) Krcha, M. D.; Mayernick, A. D.; Janik, M. J. *J. Catal.* **2012**, *293*, 103−115.
(49) Jankowiak, J.; Barteau, M. *J. Catal.* **2005**, *236*, 366−378.
(50) Salmeron, M.; Brewer, L.; Somorjai, G. A. *Surf. Sci.* **1981**, *112*, 207−228.
(51) Joyner, R. W.; Roberts, M. W.; Yates, K. *Surf. Sci.* **1979**, *87*, 501−509.
(52) Joyner, R. W.; Roberts, M. W. *Chem. Phys. Lett.* **1979**, *60*, 459−462.
(53) Bukhtiyarov, V. I.; Kaichev, V. V.; Prosvirin, I. P. *Top. Catal.* **2005**, *32*, 3−15.
(54) Knop-Gericke, A.; Kleimenov, E.; Haevecker, M.; Blume, R.; Teschner, D.; Zafeiratos, S.; Schloegl, R.; Bukhtiyarov, V. I.; Kaichev, V. V.; Prosvirin, I. P.; Nizovskii, A. I.; Bluhm, H.; Barinov, A.; Dudin, P.; Kiskinova, M. In *Advances in Catalysis*; Gates, B. C., Knozinger, H., Eds., Elsevier: Amsterdam, The Netherlands, **2009**; Vol. *52*, pp 213−272.
(55) Mai, H. X.; Sun, L. D.; Zhang, Y. W.; Si, R.; Feng, W.; Zhang, H. P.; Liu, H. C.; Yan, C. H. *J. Phys. Chem. B* **2005**, *109*, 24380−24385.
(56) Tao, F.; Zhang, S. R.; Nguyen, L.; Zhang, X. Q. *Chem. Soc. Rev.* **2012**, *41*, 7980−7993.
(57) Moulder, J. F.StickleW. F.; Sobol, P. E.; Bomben, K. D. *Handbook of X-ray Photoelectron Spectroscopy*; Perkin-Elmer Corporation: Eden Prairie, MN, 1992.
(58) Nolan, P. D.; Lutz, B. R.; Tanaka, P. L.; Mullins, C. B. *Surf. Sci.* **1998**, *419*, L107−L113.
(59) Mullins, D. R.; Overbury, S. H.; Huntley, D. R. *Surf. Sci.* **1998**, *409*, 307−319.

(60) Bancroft, G. M.; Adams, I.; Coatsworth, L. L.; Bennewitz, C. D.; Brown, J. D.; Westwood, W. D. *Anal. Chem.* **1975**, *47*, 586−588.
(61) Kim, K. S.; Gossmann, A. F.; Winograd, N. *Anal. Chem.* **1974**, *46*, 197−200.
(62) Contour, J. P.; Mouvier, G.; Hoogewys, M. *J. Catal.* **1977**, *48*, 217−228.
(63) Wen, C.; Zhu, Y.; Ye, Y. C.; Zhang, S. R.; Cheng, F.; Liu, Y.; Wang, P.; Tao, F. *ACS Nano* **2012**, *6*, 9305−9313.
(64) *Handbook of Inorganic Compounds*; Perry, D. L., Phillips, S. L., Eds.; CRC Press: Boca Raton, FL, 1995.
(65) Skriver, H. L.; Rosengaard, N. M. *Phys. Rev. B* **1992**, *46*, 7157−7168.
(66) Samsonov, G. V. *The Oxide Handbook*,. 2nd ed.; IFI/Plenum: New York, 1982.
(67) Bichowsky, F. R.; Rossini, F. D. *Thermochemistry of the Chemical Substances*; Reinhold Publishing: New York, 1936.
(68) Fu, Q.; Saltsburg, H.; Flytzani-Stephanopoulos, M. *Science* **2003**, *301*, 935−938.
(69) Blomberg, S.; Lundgren, E.; Westerstrom, R.; Erdogan, E.; Martin, N. M.; Mikkelsen, A.; Andersen, J. N.; Mittendorfer, F.; Gustafson, J. *Surf. Sci.* **2012**, *606*, 1416−1421.
(70) Grass, M. E.; Zhang, Y.; Butcher, D. R.; Park, J. Y.; Li, Y.; Bluhm, H.; Bratlie, K. M.; Zhang, T.; Somorjai, G. A. *Angew. Chem., Int. Ed.* **2008**, *47*, 8893−8896.